ACS OMEGA

http://pubs.acs.org/journal/acsodf

Article

Development of Self-Healing Carbon/Epoxy Composites with Optimized PAN/PVDF Core–Shell Nanofibers as Healing Carriers

Naga Kumar C, Prabhakar M. N.,* Mohamad Tarmizie Hassim, and Jung-il Song*

Cite This: *ACS Omega* 2022, 7, 42396–42407

Read Online

ACCESS | Metrics & More | Article Recommendations | Supporting Information

ABSTRACT: Two-component self-healing carbon/epoxy composites were fabricated by incorporating healing agents between to carbon fiber laminates via the vacuum bagging method. Vinyl ester (VE), cobalt naphthalene (CN), and methyl ethyl ketone peroxide (MEKP) were encapsulated in a polyacrylonitrile (PAN)/Poly(vinylidene fluoride) (PVDF) shell via co-axial electrospinning. Varying nanofiber compositions were fabricated, namely, 10, 20, 30, and 40% PAN in PVDF nanofibers. The 20% PAN fibers were finalized as the shell material owing to their superior tensile properties and surface morphology. The behavior of the PAN/PVDF nanofibers encapsulating the healing agents was studied via Fourier-transform infrared spectroscopy (FTIR), field emission scanning electron microscopy (FESEM), and thermogravimetric analysis (TGA) to affirm the presence of the healing agents. Mechanical analysis in the presence of core–shell nanofibers indicated an enhancement of 7 and 5% in flexural strength and Izod impact strength, respectively. Three-point bending tests confirmed the autonomous healing characteristics of these nanofibers, which retained 62% of their initial strength after 24 h. FESEM and energy dispersive X-ray (EDX) analyses of the fracture surface confirmed that the resin was released from the nanofibers, restoring the initial properties of the composites.

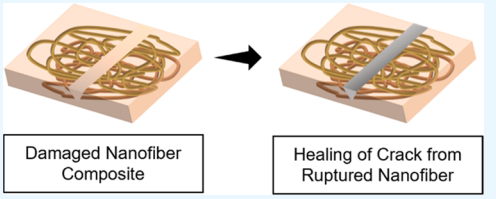

1. INTRODUCTION

The utilization of high-strength composite materials has seen substantial growth in various industrial and aeronautical applications.[1,2] However, the gradual reduction in strength and degradation of properties is customary, which is often caused by internal defects resulting from a prolonged service life. It is impossible to visually detect these defects, and nondestructive techniques, which are often laborious, are required for inspection. External damages are typically observable to the naked eye and can be repaired by patching or welding.[3,4] However, these methods are not autonomous because they require external intervention and manual work, as in the case of internal defects. These limitations have led to the development of autonomous self-healing composites, which has been a field of particular interest over the past two decades.[5,6] The fundamental self-healing mechanism can be broken down into three parts: (i) initiation from an external stimulus, (ii) flow of the healing agents into the damaged site, and (iii) chemical repair (curing) process.[7−9] Over the past years, researchers have developed two forms of self-healing composites, i.e., intrinsic- and extrinsic-based self-healing composites, which function based on the same principle.[10]

Studies on self-healing composites were first set in motion after White et al. proposed the use of microcapsules as vessels for resins in fiber-reinforced composites.[11] Subsequently, various groups branched from this study toward the utilization of containers, of varying sizes and geometries, as self-healing agent carriers for polymer composites. Studies have found microscale self-healing agent carriers to have an adverse effect on the composites, including a reduction in strength due to agglomeration and poor dispersion.[12−16] Sinha-Ray first utilized micro/nanofibers as self-healing carriers by encapsulating dicyclopentadiene (DCPD) and isophorone diisocyanate via emulsion electrospinning, wherein polyacrylonitrile (PAN) acted as the shell.[17] Nanofibers, as healing agent carriers, were widely dispersed and found to have minimal adverse effects on fiber-reinforced composites, as opposed to their microcontainer counterparts.[18−20] The popularity of nanofibers is due to their desirable mechanical and thermal properties, highly porous nature, and large surface-area-to-volume ratio. These attributes would aid in the dispersion of healing carriers throughout the composite, while ensuring a good interaction with the matrix and reinforcing fibers, without interrupting or damaging their surface morphology.[21−23]

Several research groups have focused on carbon-fiber-based self-healing composites to study the variations in their mechanical and self-healing properties. Kostopoulos et al. prepared carbon/epoxy self-healing composites by incorporating a healing resin based on the Diels–Alder reaction mechanism in targeted regions and observed a 75% extension of its fatigue life given a sufficient healing period during fatigue cyclic loading.[24] Kim et al. fabricated a carbon fiber prepregs

Received: August 26, 2022
Accepted: October 26, 2022
Published: November 9, 2022

composite with healing agents encapsulated in microcapsules, wherein healing characteristics were observed after inducing fatigue cracks in the composite. However, microcapsules act as stress raisers within the composites, leading to a decrease in the modulus compared with pure carbon-reinforced composites.[25] Hence, several studies have shifted their approach and employed core−shell nanofibers as healing agent carriers. The healing performance of carbon/epoxy composites incorporated with healing core−shell nanofibers was studied by Neisiany et al. It was found that the incorporation of core−shell nanofibers containing healing agents enabled a composite strength retention of 96 and 102% after the initial and second bending cycles.[26] Nanofibers are known to have toughening and strengthening effects on composites, and hence, Wang et al. manufactured a core−shell nanofiber-based self-healing carbon fiber composite in which the nanofibers were embedded in different sequences to study the effect of the core−shell nanofiber interlayer distribution. It was found that layering the nanofibers between each carbon fabric improved the properties of the composite, with the capability of recovering its strength after two bending loading cycles.[27] Chen et al. incorporated epoxy and its curing agent in polyamide interlayering carbon fiber laminates. An 89.96% flexural strength recovery was attained after 20 min upon curing at 130 °C.[28]

Most of the current studies focus on nanofibers, encapsulated with low-viscosity epoxy resin, as healing agents. Therefore, the current study was conducted to understand the viability of vinyl ester (VE), cobalt naphthalene (CN), and methyl ethyl ketone peroxide (MEKP) as two-part healing agents owing to their good mechanical performance, low viscosity, and low-cost relative to epoxy resins.[29] The reduced viscosity of vinyl ester, as opposed to the conventional or low-viscosity epoxy resin, would aid in its encapsulation during electrospinning, minimizing instabilities in the fabrication process. Additionally, its low viscosity would also facilitate its flow into cracks or gaps surrounding the damaged area, hastening the repair process and alleviating any further crack propagation. Poly(vinylidene fluoride) (PVDF), which is commonly used in various industries, was selected as the shell material because of its piezoelectric nature, thermal stability, chemical resistance, and mechanical strength.[30] However, its large elongation at break delays the release of encapsulated healing agents.[31] Hence, a novel PAN and PVDF blend nanofiber was utilized as the shell solution because PAN reduces the ductility of PVDF while retaining its desirable properties.[32] The composites were fabricated by layering core−shell nanofibers between each carbon fiber prepreg layer to attain symmetry while maximizing nanofiber dispersion throughout the composites. Having the nanofiber mats layered between the carbon fibers minimize the resin-rich region, hence toughening the composites as damages typically offsets from the resin-rich region. Carbon fiber prepregs are utilized because of their solvent-free epoxy resin, ease of processing, and desirable mechanical properties. The cost-effectiveness of carbon fiber prepregs has made their use widespread in the current research and industrial sectors.[33] The flexural and healing properties of the fabricated composites were studied by subjecting them to three-point bending tests and the possibility of repeated healing was also considered.

2. MATERIALS AND METHODOLOGY

2.1. Materials. The following are the materials used in this investigation, which were obtained from several companies: PVDF and PAN were procured from Sigma-Aldrich in the United States, while dimethyl formamide (DMF) (99.0%) was obtained from Samchun Chemicals in South Korea. CCP Composites, Korea, provided the VE (viscosity = 150 cps and specific gravity = 1.03), MEKP (catalyst), and CN (accelerator). SK Chemical in Korea provided carbon prepregs (USN125B, thickness: 0.12 mm).

2.2. Synthesis of Nanofibers. PAN (6 wt %) was dissolved in DMF and stirred for 8 h at room temperature, while PVDF (18 wt %) was concurrently dissolved in DMF at 80 °C. Upon complete dissolution of each solution, different amounts of the PAN solution (10, 20, 30, and 40%) were added to the PVDF solution and stirred overnight to ensure homogeneity. The prepared solutions were subjected to electrospinning, in which the nozzle tip-to-collector distance was set at 15 cm, with an applied voltage of 18 kV. Co-axial spinneret was utilized with VE-CN mixture and MEKP as core solutions supplied separately through the inner needle at a flow rate of 0.08 mL/h, while the PAN/PVDF solution was supplied through the outer needle at a flow rate of 1.0 mL/h yielding nanofiber mats with a thickness of 35−50 μm.

2.3. Fabrication of Self-Healing Composites. Three different composite compositions were fabricated in this study via vacuum bagging, namely, the control composite (CCP), composite with nanofibers without a healing agent (WOHP), and core−shell nanofibers with healing agent-reinforced composites (WHP). CCP composites were fabricated by laminating the prepregs with a sequence of [0, 90, 90, 0]. The prepregs were then covered with a peel ply and a breather layer to avoid excess resin in the composite. A double-sided sealant tape was attached around the fabric, and the entire setup was covered with a vacuum bag with an output connected to a vacuum pump. The setup was vacuumed and subsequently cured in a curing oven at 80 °C for 15 min and then at 125 °C for an hour. WOHP composites were fabricated by layering each carbon fiber prepregs with PAN/PVDF monolithic nanofibers, while the WHP composites were layered with core−shell nanofibers carrying the healing agents.

2.4. Tests and Characterizations. The nanofiber mats with dimensions of 25 mm × 15 mm were subjected to tension on a Universal Testing Machine (UTM) (2.5-ton load, R&B, Inc., South Korea) with a crosshead speed of 1 mm/min. The attenuated total reflectance (ATR)-Fourier-transform infrared spectroscopy (FTIR) spectra of nanofibers were attained using a Fourier transform infrared (FT-IR-6300, JASCO International Co., Ltd., Japan) spectrometer, and the FTIR spectra were collected over 4000−400 cm^{-1}. Thermal analysis was performed on a thermogravimetric analyzer (STA 6000, PerkinElmer, U.K.) at a heating rate of 20 °C/min over 30−700 °C with a constant supply of nitrogen. Flexural tests of the composites were performed on a computerized UTM machine (10-ton load, R&B Inc., South Korea) at a crosshead speed of 2 mm/min in compliance with ASTM D-790 standards. An Izod impact test was performed on the composites using an Izod impact testing machine (model QC-639F, Cometech, Korea) with a 22 J capacity in accordance with ASTM D-256 standards. The surface morphologies of the nanofibers and fracture surfaces of the composites were examined using field emission scanning electron microscopy (FESEM) (LYRA3xm, Czech Republic) at an acceleration voltage of 10 kV coupled with an energy-dispersive X-ray (EDX) analyzer for elemental analysis. The samples were sputter-coated with gold using an

https://doi.org/10.1021/acsomega.2c05496
ACS Omega 2022, 7, 42396−42407

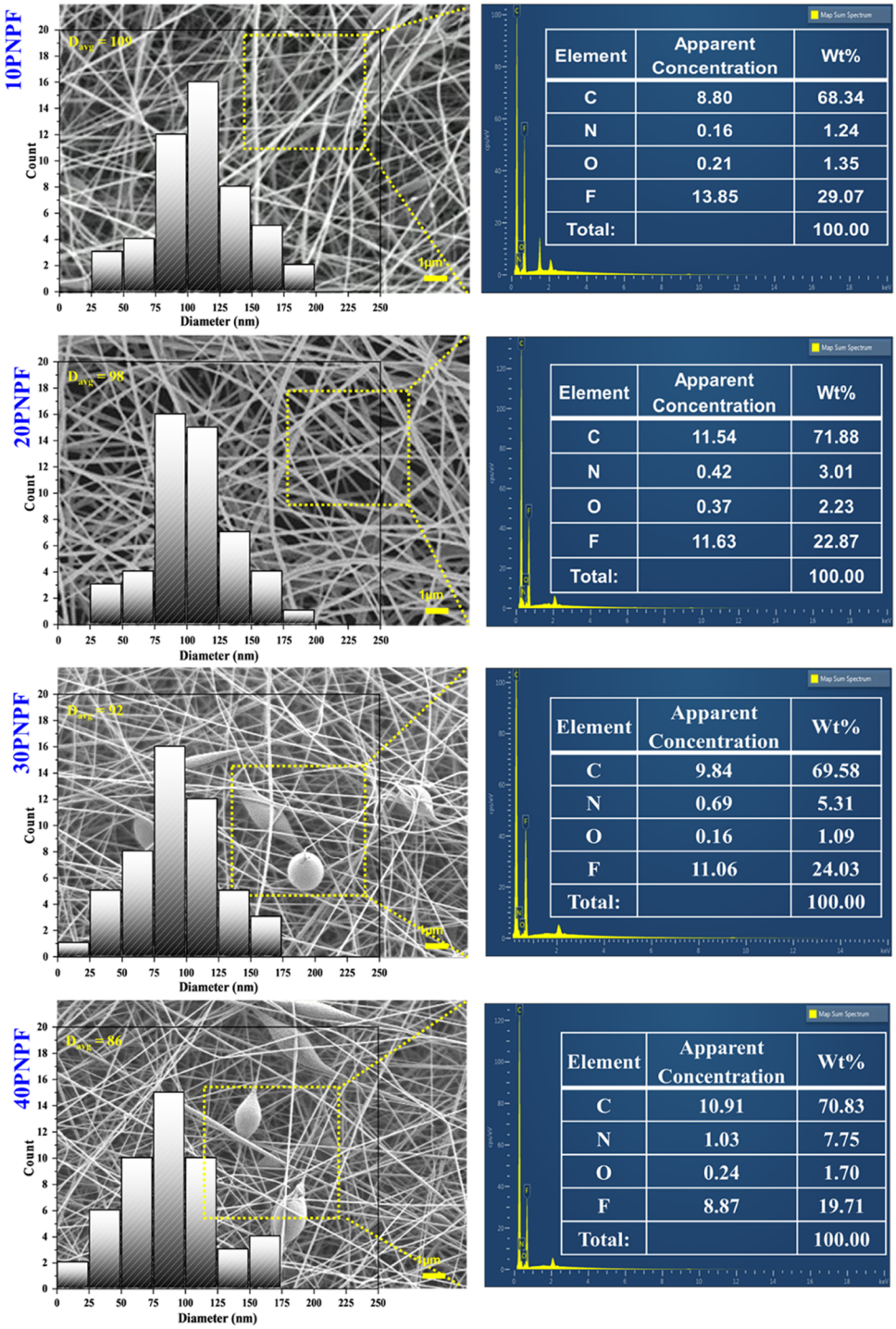

Figure 1. PAN/PVDF nanofibers: (A) FESEM images with diameter distribution histogram at low magnification and (B) EDX analysis.

automated fine coater (JEOL JFC-1600) prior to the morphological study.

3. RESULTS AND DISCUSSION

3.1. Morphological Studies of Core−Shell Nanofibers.

FESEM coupled with EDX was used to study the morphological structure, elemental composition, and nanofiber diameter of varying compositions of the PAN/PVDF nanofiber mats, as shown in Figure 1 (pure PVDF and PAN as shown in Supporting Section). All of the PAN/PVDF composites were successfully spun, forming randomly oriented fibrous mats as a conventional flat collector. It was observed that the neat PVDF nanofibers had the largest diameter with a constant decrease in diameter observed as the PAN concentration increased. The average diameters of the PVDF, 10PNPF, 20PNPF, 30PNPF, 40PNPF, and PAN nanofibers were 115, 109, 98, 92, 86, and 74 nm, respectively.

The decrease in diameter is attributed to the low PAN content in the solution (6%), yielding thinner fibers as more solvents are evaporated mid-flight. The change in diameter of the nanofibers with the change in PAN weight percentage is shown in the distribution diagram in Figure 1A. Smooth fibers

https://doi.org/10.1021/acsomega.2c05496
ACS Omega 2022, 7, 42396−42407

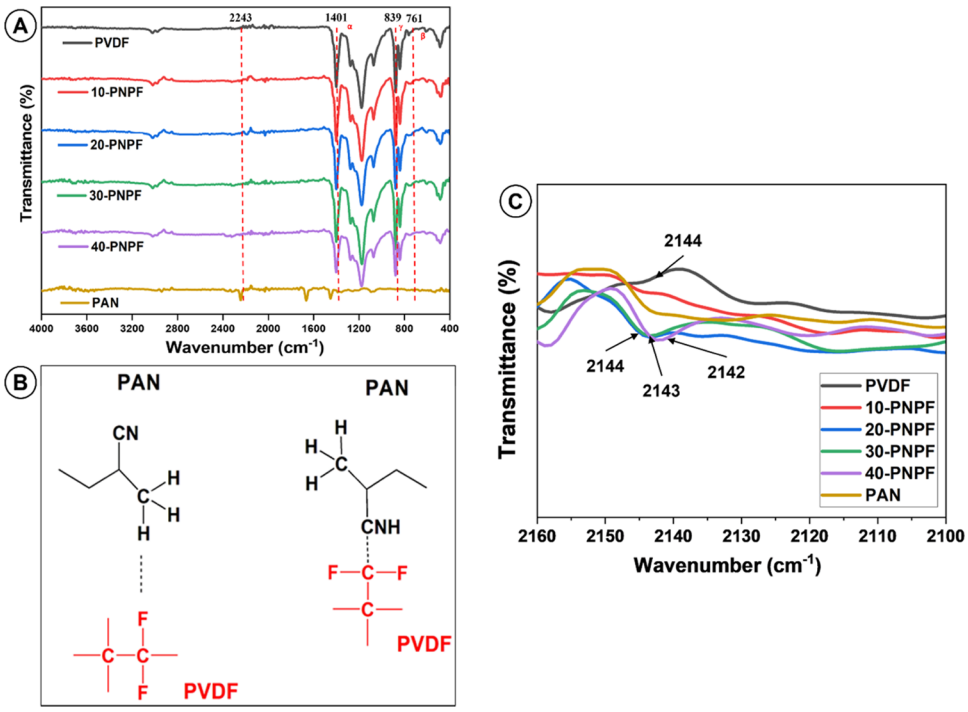

Figure 2. (A) Overall spectra of PAN/PVDF nanofibers, (B) proposed molecular interaction between PAN and PVDF, and (C) designation of new peaks.

were fabricated for the PVDF, PAN, 10PNPF, and 20PNPF specimens, with a uniform thickness, whereas micro-sized beads were observed for the 30PNPF and 40PNPF solutions. Despite the utilization of DMF in both polymer solutions, the considerable difference in the polymer concentration affected the evaporation rate of the solvents. The 6% PAN solution would have a relatively slower evaporation rate than the 18% PVDF solution because of the increased solvent content in the solution. Hence, the formation of beads-on-fiber at elevated PAN contents may be attributed to the difference in the evaporation rates of the two solutions. Figure 1C shows that the changes in the polymer blend with increasing PAN content exhibited a notable increase in nitrogen content and a reduction in fluoride as the PAN concentration increased.

3.2. Spectral Analysis of Nanofibers. Figure 2 shows the spectral analysis of the PAN/PVDF nanofibers. The orthorhombic α (α), β (β), γ (γ), and monoclinic delta (δ) phases are well-known crystalline structures of PVDF, with their formation depending on the crystallization conditions. Here, the polymorphism of pure PVDF shows the crystalline phases of PVDF and can be identified through the characteristic vibrational modes between 1400 and 600 cm $^{-1}$. The ATR-FTIR spectra exhibited bands at 761, 612, and 406 cm^{-1} corresponding to the characteristics of the α phase. The vibrational modes of the β phase were assigned to 1401, 1277, 1175, 1071, 510, 486, and 444 cm^{-1}. However, a γ phase is observed at 839 cm^{-1} as shown in Figure 2A.[34−36] In PAN, peaks of interest were observed at 2243 cm^{-1}, assigned to the stretching vibration of C−N (triple bond), and 1558 cm^{-1}, assigned to the stretching vibration of C═C conjugated with C═N. Other characteristic peaks, such as the weak stretching of hydroxyl groups (−OH−) at 3111 cm^{-1}, and the stretching and bending vibrations of methylene (−CH_2−) at 1453 cm^{-1}, were observed. The peaks at 1256 and 1354 cm^{-1} were assigned to the aliphatic CH group vibrations of different modes in CH and CH_2, respectively.[37]

FTIR spectral analysis of the PVDF, PAN, and PVDF/PAN nanofibers confirmed the interaction between the −CN group of PAN and the F atom of PVDF. A positive σ-hole is found when fluorine is linked to N or C atoms bearing particularly strong electron-withdrawing substituents.[38] Thus, this interaction forms a halogen bond (XB), which is defined as a noncovalent attractive interaction between an electrophilic region (σ-hole) on an XB-donating halogen atom and a Lewis base that functions as an XB acceptor. The proposed CH−CF and CN−CF interactions are shown in Figure 2B.

As a result of the PAN/PVDF interaction, the C≡N bond was weakened, and the peak at 2243 cm^{-1} shifted to lower wavenumbers (i.e., higher frequency). A new peak at 2142−2144 cm^{-1} appeared, which indicates the presence of two types of C≡N in the PVDF/PAN blend, as shown in Figure 2C. This means that some of the nitrile groups were free and appeared at 2243 cm^{-1}, while others that interacted with halogens appeared at 2140 cm^{-1}.[39] The gradual addition of PAN to PVDF indicates that cyclization reactions that turn −C≡N− groups into a −C═N− structure have occurred. The intensity of the bands at 2700, 2140, 1300, 1200, and 700−800 cm^{-1} increases significantly with the increase in the blend, suggesting that intermolecular reactions that convert the −CH_2−CH− structure into the −CH═C− structure have occurred. Likewise, it is commonly recognized that the electron density distribution around a free halogen atom in its ground state is, on average, spherically symmetrical because the contribution of the nucleus dominates that of the dispersed electrons. This is a real physical property of a system that is quite effective in predicting noncovalent interactions.[38]

3.3. Thermal Analysis and Core Content of Nanofibers. Thermogravimetric analysis was conducted to study the effects of blending PVDF with the PAN solution on the

https://doi.org/10.1021/acsomega.2c05496
ACS Omega 2022, 7, 42396−42407

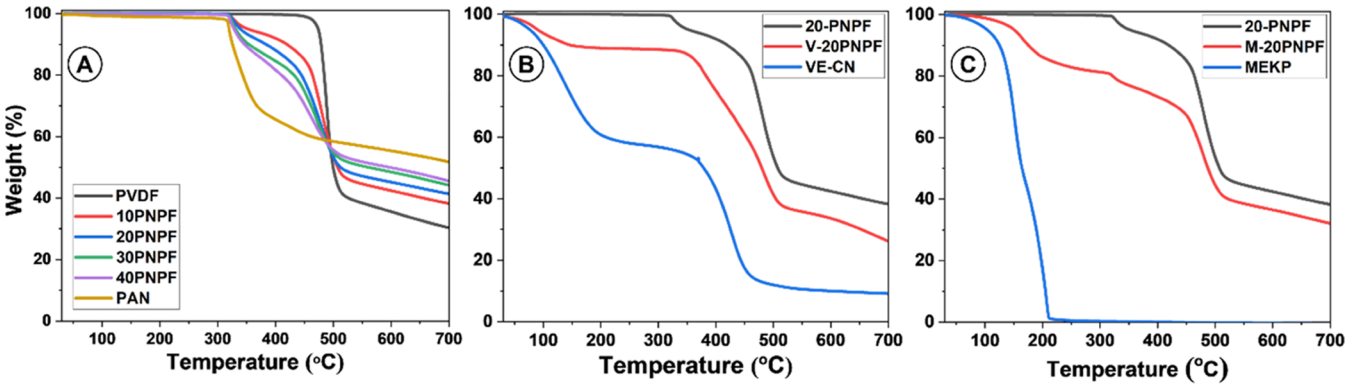

Figure 3. Thermographs of (A) PAN/PVDF, (B) V-20PNPF, and (C) M-20PNPF nanofibers.

Table 1. TGA and Tensile Test Results of PAN/PVDF Nanofibers

	TGA results			tensile test		
name of the specimen	T_{onset} 10% (C)	T_{onset} 50% (C)	residue (wt %)	tensile strength (MPa)	tensile modulus (MPa)	elongation at break (%)
PVDF	470	520	30.0	2.33 ± 0.12	36.85 ± 3.4	64 ± 3.08
10PNPF	420	510	38.2	2.42 ± 4.60	38.20 ± 4.6	58 ± 2.30
20PNPF	380	510	41.3	2.75 ± 0.18	42.60 ± 4.8	52 ± 3.50
30PNPF	350	560	44.2	2.61 ± 0.09	41.80 ± 3.3	50 ± 2.90
40PNPF	340	600	45.6	1.80 ± 0.11	32.34 ± 2.4	38 ± 2.70
PAN	330	700	52.8	2.50 ± 0.15	48.50 ± 3.8	41 ± 3.30

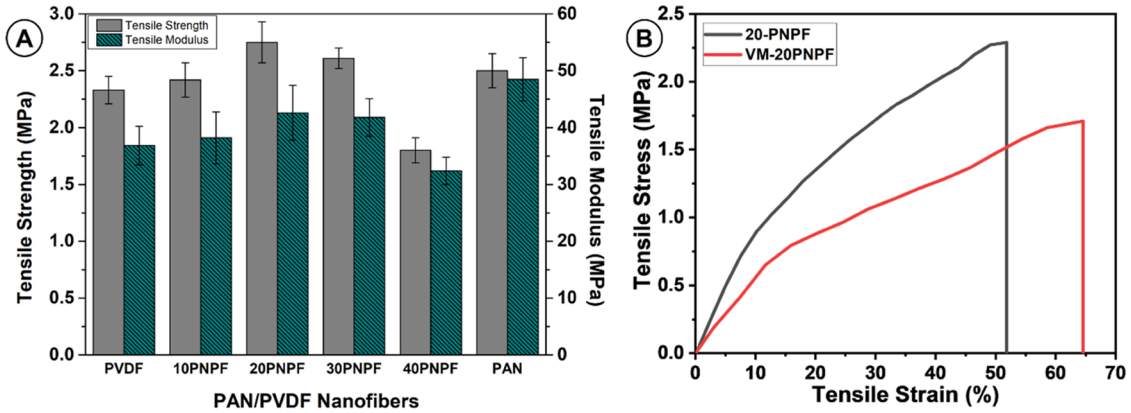

Figure 4. (A) Tensile properties of PAN/PVDF nanofibers. (B) Stress−strain graph of 20PNPF and VM-20PNPF nanofibers.

thermal stability of the resulting nanofibers. The thermal curves of PVDF, PAN, and PAN/PVDF nanofibers are shown in Figure 3A, and T_{onset} and T_{max} are listed in Table 1. Heating the samples to 700 °C under ambient conditions yielded weight residues of 30, 38.25, 41.39, 44.2, 45.62, and 52.8% for PVDF, 10PNPF, 20PNPF, 30PNPF, 40PNPF, and PAN, respectively, as listed in Table 1. The presence of PAN notably improved the thermal stability of the blend solution, as PAN exhibited superiority in weight residue at 700 °C. Figure 3A shows that PVDF experienced a major weight loss of 60%, from 450 to 500 °C, whereas PAN nanofibers exhibited a much more gradual weight loss, from approximately 310 °C up to 500 °C. The PAN/PVDF blend solution exhibited traits of both its individual constituents, with a degradation initiation similar to that of the PAN nanofibers, degrading over a broader range of temperatures with an improvement in its weight residue relative to the PVDF nanofibers. The improvement in the thermal stability of PAN/PVDF was evident, as these traits are more prominent with increasing PAN concentration in the blend solution.

The thermogravimetric analysis (TGA) curves of the core−shell nanofibers, namely, 20PNPF, V-20PNPF, and VE-CN, are plotted in Figure 3B. Thermogravimetric analysis of the core−shell nanofibers confirmed the encapsulation of VE-CN and determined the encapsulated core content in the nanofibers. 20PNPF degrades between 320 and 515 °C with a final mass residue of 38%. The TGA curve of VE-CN exhibited two distinct mass loss steps. The first stage started below 100 to 200 °C, while the second stage started at 360 °C and ended at 500 °C. As the V-20PNPF specimen comprised VE-CN encapsulated by 20PNPF, the thermal degradation curve of V-20PNPF had the characteristics of both components. Notably, approximately 10% of the mass was lost from 100 to 200 °C, indicating the degradation of VE-CN, followed by further mass loss from 320 °C, which reflected the degradation of the PAN nanofiber shell. The mass loss of V-20PNPF from 320 to 500 °C was notably higher than that of 20PNPF, implying that rapid mass loss is a result of the degradation of both 20PNPF and the second-step mass loss of VE-CN. Consequently, the difference between the weight

https://doi.org/10.1021/acsomega.2c05496
ACS Omega 2022, 7, 42396−42407

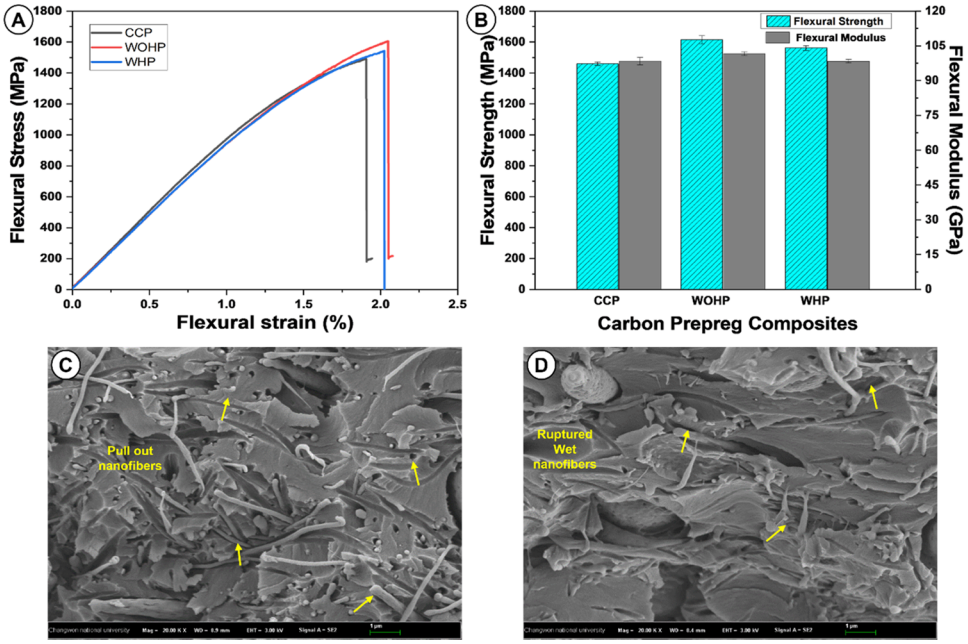

Figure 5. (A) Flexural stress−strain graphs; (B) strength and modulus of CCP, WOHP, and WHP composites; and SEM images of (C) WOHP and (D) WHP fractured surface.

residue of 20PNPF and V-20PNPF at 420 °C determined the volume percentage of encapsulated VE-CN to be 20%. Figure 3C shows the thermal degradation behavior of 20PNPF, M-20PNPF, and MEKP. MEKP exhibited a rapid mass loss between 100 and 210 °C, leaving almost no residue after 210 °C. For the 20PNPF core−shell nanofiber containing MEKP (M-20PNPF), the general thermal degradation pattern occurred between 100 and 500 °C, which consisted of two different stages. M-20PNPF started losing mass at 100 °C but retained 82% of its initial weight after 210 °C, which is attributed to the complete deterioration of the MEKP. Using the same approximation, the MEKP content encapsulated in M-20PNPF was calculated to be 18% at 210 °C.

3.4. Optimization of PAN/PVDF Nanofibers through Tensile Properties. The variation in the tensile properties with the introduction of PAN into PVDF was investigated by performing tensile tests on PAN, PVDF, and PAN/PVDF nanofibers. Table 1 lists the tensile strength, modulus, and elongation at break of the PAN/PVDF nanofiber mats. The tensile strength of PVDF, 10PNPF, 20PNPF, 30PNPF, 40PNPF, and PAN nanofibers were 2.3, 2.4, 2.8, 2.6, 1.8, and 2.5 MPa, respectively, as shown in Table 1. The strength of the PVDF nanofibers increased with an increase in the weight percentage of PAN, peaking at 20 wt % PAN content, followed by a decline in strength, as shown in Figure 4A. The increase in strength with the addition of PAN was attributed to the good interaction between PAN and PVDF, as discussed previously in the FTIR analysis section. Conversely, the observed decrease in the tensile strength of 30PNPF and 40PNPF was due to the low viscosity of these precursor solutions. As the PAN concentration in the PAN/PVDF blend solution increased, the solution comprised more DMF solvents, which diluted it, yielding nonuniform and beaded fibers. These defects act as stress raisers in the nanofiber mats, causing a significant reduction in their strengths, which was especially evident in the 40PNPF mats, which exhibited a decrease in strength of 23 and 28%, with respect to the PVDF and PAN nanofiber mats, respectively.

The tensile moduli of the PVDF, 10PNPF, 20PNPF, 30PNPF, 40PNPF, and PAN nanofibers were 36.8, 38.5, 42.6, 41.8, 32.3, and 48.5 MPa, respectively, as shown in Table 1. The modulus of the nanofibers showed a similar trend to that of tensile strength, whereby an improvement in the modulus was observed with an increase in PAN up to 20 wt %, followed by a decrease as the PAN concentration exceeds 20 wt %, as shown in Figure 4A. PAN nanofibers exhibited superiority, in terms of the modulus, among all of the nanofibers. Hence, the introduction of PAN into PVDF increased the strength and modulus of the blended nanofibers. PAN has a semicrystalline structure with a moderate degree of crystallinity, which is attributed to its higher modulus and hardness. These desirable traits of PAN enhanced the moduli of 10PNPF and 20PNPF when it was added to PVDF. The modulus began to decline when the solution was predominantly composed of PAN, as shown in Figure 4A, due to defective nanofibers at these compositions. Similarly, the elongations at break of PVDF, 10PNPF, 20PNPF, 30PNPF, 40PNPF, and PAN nanofibers were 64, 58, 52, 50, 38, and 41%, respectively, as shown in Table 1. The implications of the PAN concentration are akin to those of the tensile properties, as the elongation at break is correlated to the tensile strength and modulus. PVDF nanofibers are more ductile with high tensile strain, whereas PAN, a relatively brittle polymer, elongates less prior to fracture. The elongation at break of the PVDF/PAN blend nanofibers was reduced compared to that of the neat PVDF nanofibers because PAN is known to have better crystallinity. Evidently, the ductility of PVDF can be alleviated by blending it with PAN solution. Considering the tensile properties of these nanofibers, 20PNPF was utilized as the shell solution for fabricating core−shell nanofibers.

The tensile properties due to the presence of the core solution were also studied by subjecting self-healing nanofiber mats (VM-20PNPF), consisting of V-20PNPF and M-20PNPF

https://doi.org/10.1021/acsomega.2c05496
ACS Omega 2022, 7, 42396−42407

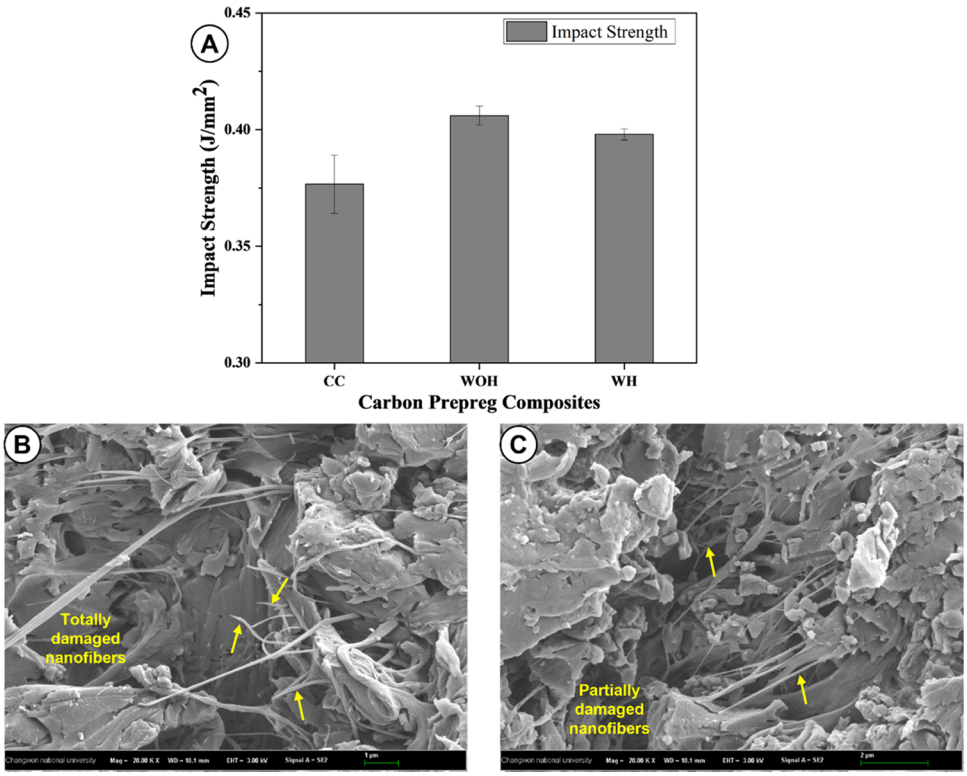

Figure 6. (A) Izod impact strengths of CCP, WOHP, and WHP composites. SEM images on fractured surface of (B) WOHP and (C) WHP composites.

layers, to tensile load. Figure 4B shows the stress−strain curves of both 20PNPF and VM-20PNPF. The thickness of the self-healing nanofibers mats was almost double that of the monolithic nanofibers owing to the presence of the core material yielding thicker fibers. The tensile strength of VM-20TPn was 1.7 MPa with a modulus of 32.5 MPa. The tensile strength and modulus of VM-20PNPF were inferior to those of 20PNPF because they contain a liquid core (VE-CN and MEKP), reducing its strength and modulus. Figure 4B also shows the well-known regimes of deformation within the stress−strain curves, which are the elastic, intermediate plastic, and ultimate catastrophic failure zones. The curves showed that elasticity up to 30% of the strain range and between 30 and 60% consists of the intermediate zone, and the rest is considered as the ultimate catastrophic failure zone. These regimes are typical of different nanofiber mats.

3.5. Mechanical Properties of Self-Healing Composites. Flexural tests were conducted to study the effects of layering nanofibers of carbon prepreg composites. The flexural strengths of CCP, WOHP, and WHP were 1459.3, 1614.7, and 1561.9 MPa, respectively. The introduction of both neat and core−shell nanofibers enhanced the flexural properties of the carbon prepreg composite by 11 and 7%, respectively. The stress−strain curve in Figure 5A shows a slight increase in the strain at break with the incorporation of nanofibers into the composites. Nanofiber mats typically consist of very long thin fibers intertwined with one another, which act as a secondary load bearer after the carbon fibers, delaying the failure of the composite, as seen in the slight increase in the flexural properties. The scanning electron microscopy (SEM) images in Figure 5C,D show the fractured surfaces of the composites with nanofibers layers, which clearly show that the incorporation of core−shell nanofibers between the laminates had a positive effect on the flexural strength. The solid bonding of the nanofibers to the epoxy resin can be attributed to the high specific surface area of the nanofibers, as their diameters are significantly smaller than those of the carbon fibers. Additionally, the core−shell nanofibers can break or detach from the epoxy resin matrix upon loading, which dissipates strain energy, causing a delay in the failure of the composite. The flexural moduli of CCP, WOHP, and WHP composites were 98.4, 101.6, and 98.4 GPa, respectively, and the variations are similar to the flexural strength as shown in Figure 5B.

The interlaminar surfaces (Figure 5C,D) of the WOHP and WHP composites showed that deformation and fracture typically occur in the interlaminar regions surrounding the nanofibers. The presence of nanofibers refracts the micro-cracks, forcing them to undergo a complicated path, thereby increasing the resistance of the composite to crack propagation. When the cracks break away from the nanofibers, they create abnormal fracture surfaces, suggesting greater dissipation of strain energy. The breakage and pullout of nanofibers play an important role in improving the strength and modulus of composites reinforced with nanofibers.

Izod impact tests were performed on the specimens to examine the fracture behavior of the carbon prepreg composites, with and without nanofibers, by measuring the energy absorbed by the composites upon impact. The impact strengths of the CCP, WOHP, and WHP composites were 0.38, 0.41, and 0.39 J/mm^2, respectively, as shown in Figure 6A. The impact absorption energy was higher for the WOHP and WHP composites than for CCP, exhibiting a similar trend to its flexural properties. The improvement in the absorption energy was similar because of the presence of nanofibers in the WOHP and WHP composites, which alleviated crack propagation in a single direction, as shown in Figure 6B,C.

https://doi.org/10.1021/acsomega.2c05496
ACS Omega 2022, 7, 42396−42407

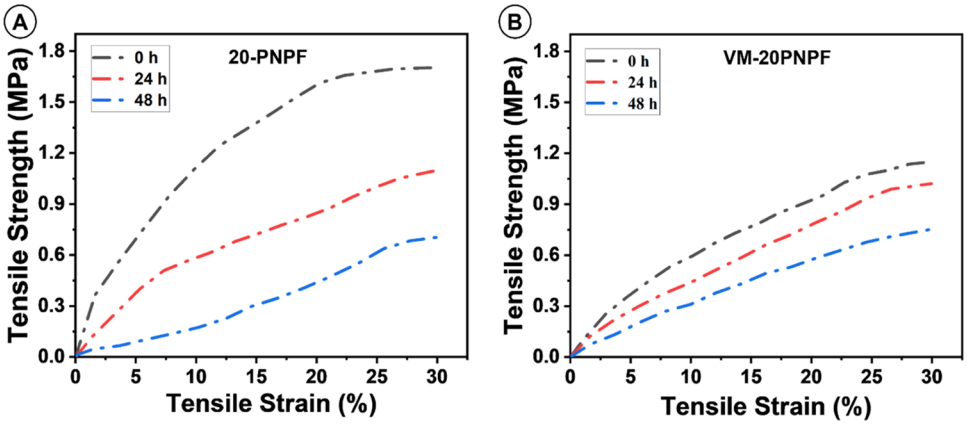

Figure 7. Stress−strain curves measured during tensile testing with a strain range of 30% (elastic zone) for (A) 20PNPF and (B) VM-20PNPF nanofibers.

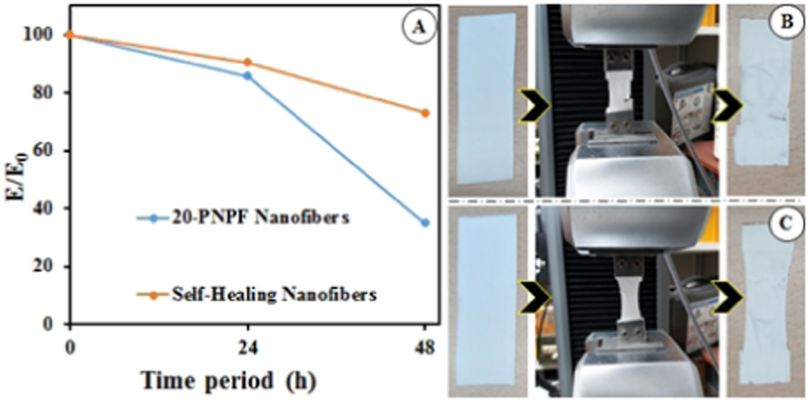

Figure 8. (A) Tensile modulus variation of 20PNPF and VM-20PNPF. Specimens before and after the third tensile stretch of (B) 20PNPF and (C) VM-20PNPF nanofibers.

The nanofibers in the composites were damaged and deviated from crack propagation, thus increasing the impact absorption energy.

3.6. Self-Healing Properties. *3.6.1. Healing Properties of Nanofibers through Tensile Testing.* Tensile tests on the nanofibers were performed up to a 30% strain rate, considering its elastic zone on 20PNPF and VM-20PNPF, at intervals of 24 h (0, 24, and 48 h) to examine the healing effect, as shown in Figure 7. The tensile strength of 20PNPF at 0, 24, and 72 h of stretching was 1.7, 1.1, and 0.7 MPa, respectively, as shown in Figure 7A. The tensile strength of VM-20PNPF at 0, 24, and 72 h was 1.1, 1.0, and 0.8 MPa, respectively, as shown in Figure 7B. The modulus of 20PNPF at the first, second and third stretching modes was 42.6, 27.9, and 9.8 MPa, respectively, whereas the modulus of VM-20PNPF was 35.5, 32.1, and 25.9 MPa, respectively. Upon stretching up to a 30% strain rate, the fibers were partially damaged and returned to their original shape upon unloading, which was then left for 24 h prior to subsequent stretching. During the second tensile test, the stress−strain curve of 20PNPF indicated significant reductions of 36 and 35% in the tensile strength and modulus, respectively. In contrast, the tensile strength and modulus of VM-20PNPF decreased by 11 and 10%, respectively. Thus, the large discrepancy between the first and second loading of the 20PNPF indicated that there is no self-healing, whereas a healing effect was observed in VM-20PNPF since the strength loss was minimized, as shown in Figure 7.

The healing effect was further confirmed by comparing the modulus variations of both nanofiber mats, as shown in Figure 8A. The modulus variation (E/E_o) was calculated by considering the modulus of the first stretching as the numerator (E), and the modulus after subsequent loading as the denominator (E_o). The modulus variations of 20PNPF and VM-20PNPF were reduced by 77 and 27%, respectively. This variation in the modulus was due to the presence of a self-healing agent embedded in VM-20PNPF, whereby the encapsulated healing agents were released upon damage to its shell, repairing any defects that minimize losses in its properties. Meanwhile, 20PNPF showed no improvement in its modulus owing to the absence of a healing agent. A notable difference was observed during the third loading cycle, whereby the 20PNPF had significant damage following the loading, whereas the VM-20PNPF was elongated without significant damage, as shown in Figure 8B,C. The significant damage to the 20PNPF was caused by the preexisting damage from the second loading and because it does not have any healing capabilities, the microcracks propagated further, causing significant damage to the mat. However, the prior damage in the VM-20PNPF was likely minimized 24 h after the second loading due to the curing of the self-healing agents upon release from the container.

3.6.2. Healing Properties of Composites through Flexural Test. The self-healing properties of the CCP and WHP composites were evaluated using periodic flexural tests conducted with a loading interval of 24 h. The composites

https://doi.org/10.1021/acsomega.2c05496
ACS Omega 2022, 7, 42396−42407

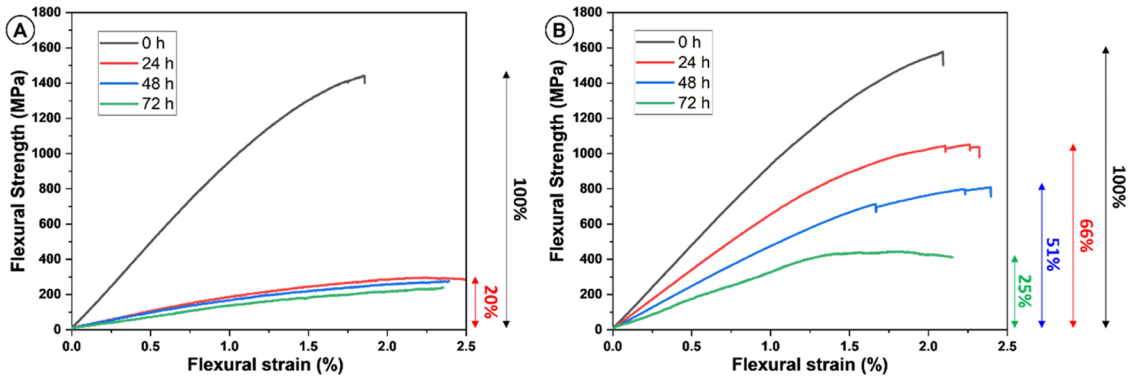

Figure 9. Flexural stress−strain curves of (A) CCP and (B) WHP composites at 24 h interval.

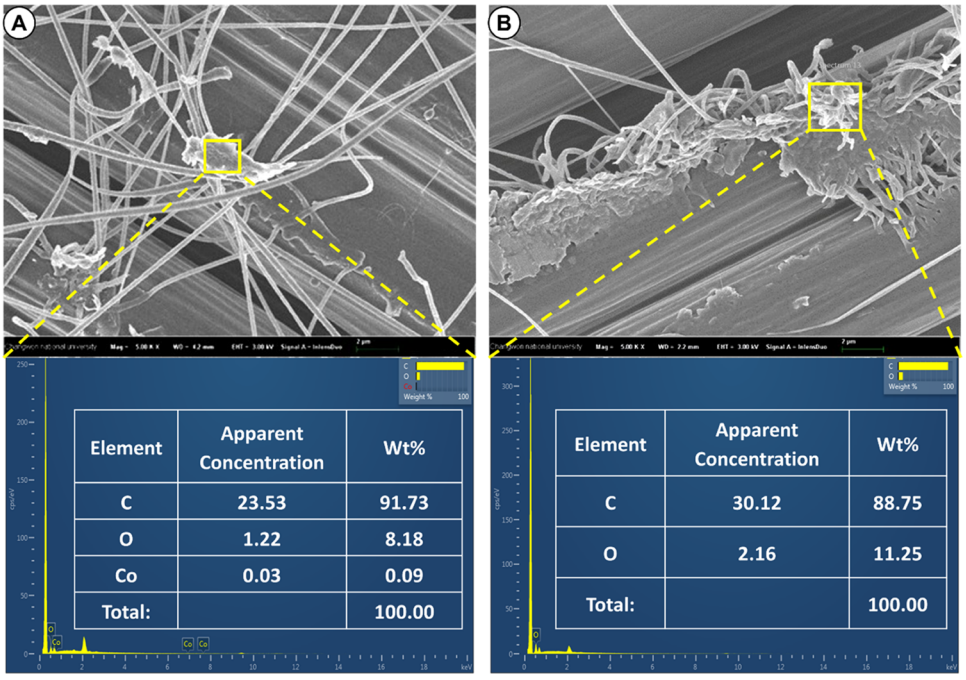

Figure 10. FESEM images and their EDX analysis at ruptured portions of (A) V-20PNPF and (B) M-20PNPF nanofibers.

were subjected to flexural loading and left untouched for 24 h to allow sufficient time for complete curing of the self-healing agents. Upon subjecting the composites to a bending load, defects within the composite, such as cracks or fiber breakage, act as initiators, causing the core−shell nanofibers to rupture. The two-part healing agent flows through the microcracks or openings and solidifies upon contact with each other to repair the damage site. Figure 9 shows the repeated flexural stress−strain curves of the composites with and without core−shell nanofibers. The flexural strengths of CCP and WHP composites were 1441.7 and 1577.9 MPa, respectively, in the first load cycle, as shown in Figure 9A,B. Both composites were tested until visible cracks were observed throughout the thickness of the composites in conjunction with a significant dip in the stress−strain curve. During the second loading, the CCP composite lost a significant chunk of its initial flexural strength, retaining only 20%, whereas the WHP composite preserved 62%, as illustrated in Figure 9A,B. The resurgence in the flexural properties of the WHP composite was apparent because of the self-healing properties of VM-20PNPF. The composites were then subjected to another load cycle 48 h after the initial loading, in which the WHP composite lost approximately half of its strength from the previous loading, resulting in a retention of 35% of the original strength. The CCP composites exhibited a similar property to the previous load cycle with a negligible decrement in the properties. Further loading cycles on the WHP exhibited no recovery in strength, as shown in Figure 9B, whereby the residual flexural strength was similar to that of the CCP composite. The absence of strength recovery may be due to two reasons: the depletion of healing agents in the core−shell nanofibers or the nanofibers surrounding the damage site did not rupture, disabling any flow of the self-healing agents.

3.6.3. Morphological Evidence. V-20PNPF and M-20PNPF were synthesized separately on a carbon fiber fabric to examine the presence of the healing agent inside the core−shell nanofibers. The nanofibers were scratched with a needle and the ruptured portions were observed using FESEM. Figure 10A,B clearly shows the release of VE-CN and MEKP from the ruptured V-20PNPF and M-20PNPF. An EDX analyzer coupled with FESEM was utilized on the area surrounding the ruptured nanofibers, which showed the presence of C, O, and Co. These are the primary elements in VE-CN, indicating the release of these core solutions, as illustrated in Figure 10A.

https://doi.org/10.1021/acsomega.2c05496
ACS Omega 2022, 7, 42396−42407

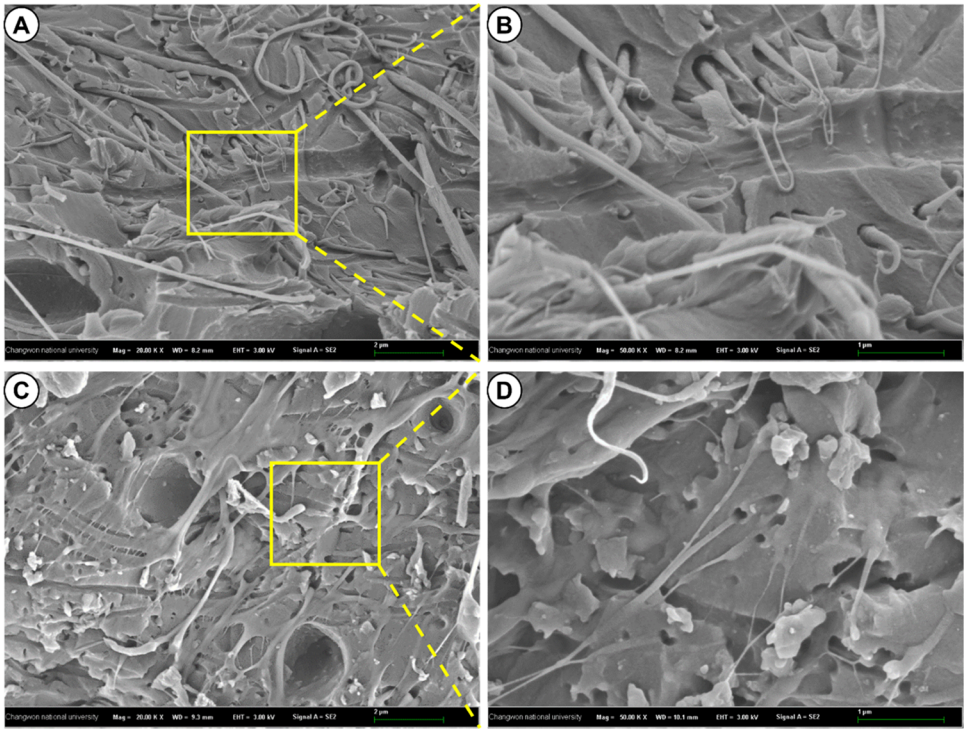

Figure 11. (A, C) FESEM images of fractured surface of WHP composites. (B, D) Higher magnification of (A) and (C).

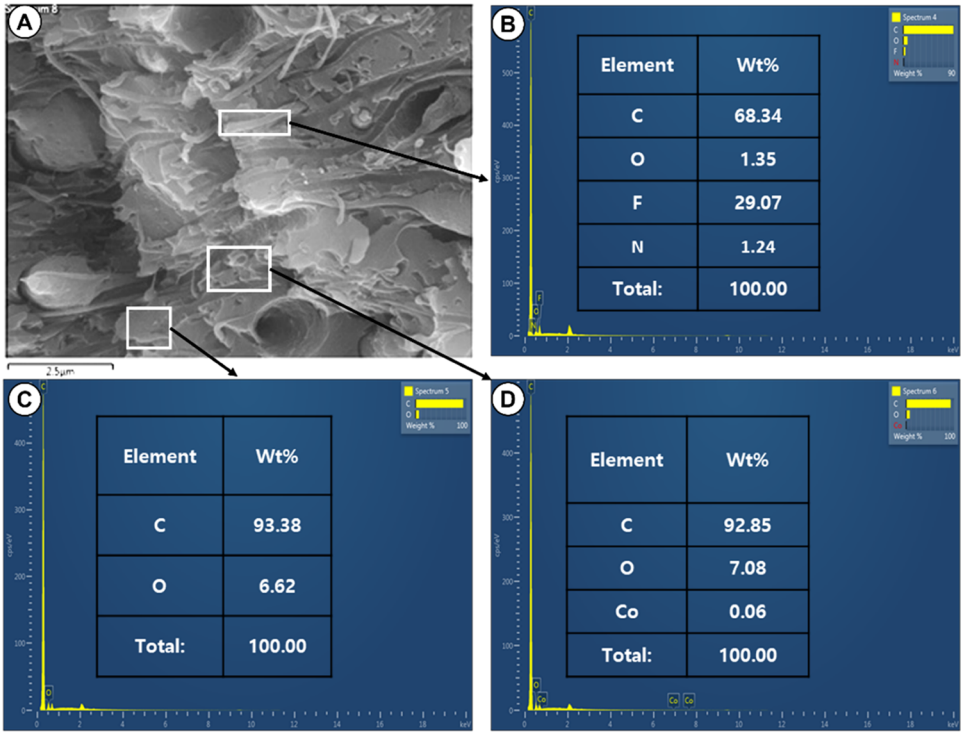

Figure 12. (A) FESEM Image of fractured surface. (B) EDX analysis of PAN/PVDF nanofibers. (C) EDX analysis of epoxy matrix. (D) EDX analysis of healing agents.

Similarly, the ruptured M-20PNPF and its core (MEKP) in the ruptured portion are shown in Figure 10B. MEKP mainly comprises C and O elements, as confirmed by EDX analyses, suggesting the presence of MEKP in the ruptured portion of M-20PNPF. Thus, when both V-20PNPF and M-20PNPF were fabricated on the same surface and ruptured, both core solutions were released from the nanofibers and solidified upon mixing, healing the damage sites.

The healing mechanism of the composites was investigated by observing the fractured surfaces of the self-healing composites by FESEM. Figure 11 shows the FESEM images of the WHP composite at the fractured portion 24 h after the first bending. Figure 11A,B illustrates the damaged nanofibers

https://doi.org/10.1021/acsomega.2c05496
ACS Omega 2022, 7, 42396−42407

releasing self-healing agents. The constituents of the healing agents, the resin, and its catalyst would flow into a gap and interact with each other. This interaction eventually leads to solidification, as observed in Figure 11C,D. Furthermore, EDX analysis was performed on the fractured surfaces to confirm the presence of VE-CN, MEKP, and PAN/PVDF nanofibers, to ensure the presence of each constituent at the damage site. Figure 12A shows the FESEM image of the WHP composite fracture surface, where all of the components are visible for EDX analysis. Figure 12B shows the elemental graph and weight percentages of the different elements contained in PAN/PVDF. C, O, F, and N were prominently present on the fracture surface, confirming the presence of nanofibers. The matrix of the composite was epoxy, which contains C and O, as shown in Figure 12C. The solidified healing agents comprise VE, CN, and MEKP, which contain C, O, and Co, as shown in Figure 12D. Thus, the EDX analysis confirmed the presence of elements in the components of the WHP composite.

4. CONCLUSIONS

In an effort to minimize crack propagation and extend the service life of a carbon fiber-reinforced composite, this work successfully prepared a novel PAN/PVDF core−shell nanofiber, consisting of a VE-CN and MEKP core, with viable self-healing capability. The tensile strength and modulus of the 20PNPF blend were found to be superior for all of the various wt % PAN/PVDF nanofibers and were utilized as the shell solution owing to their desirable morphology, good thermal stability, and tensile properties. Self-healing high-strength carbon prepreg composites, incorporated with PAN/PVDF core−shell nanofibers as healing carriers, were successfully fabricated via the vacuum bagging method. The FESEM images represent the surface morphology, size, and shape of the nanofibers and changes in diameter and elements with the addition of PAN, and also visually confirm the release of the healing agent from the core−shell nanofibers. Repeated tensile stretching concluded that the presence of the healing material in the cores of the PAN/PVDF nanofibers enabled the nanofiber to regain a significant portion of its tensile properties despite being damaged. Carbon prepreg composites with and without core−shell nanofibers were tested for their mechanical and self-healing properties. The presence of nanofibers between the carbon prepreg layers led to improvements of 11 and 7% in flexural and Izod impact strengths, respectively. The presence of nanofibers, nanofiber pullout, and damage to the core−shell nanofibers within the interlayers of the composites was confirmed through FESEM images. Furthermore, flexural tests were conducted to examine the self-healing abilities of the composites, whereby the composites could retain a reasonable portion of their flexural properties after two loading cycles, given sufficient time to cure; 62% of its original strength was regained upon the first damage of the self-healing composites owing to the presence of healing carriers (core−shell nanofibers). The FESEM images of the fractured surface of the self-healing composites also clarify the flow of the healing agent from the ruptured nanofibers into the gaps, which eventually solidifies. In addition, the incorporation of core−shell nanofibers between the carbon prepregs did not adversely affect the mechanical properties of the control composite. Hence, the fabricated self-healing composites can be utilized in industrial and structural applications without compromising their mechanical properties. Further studies can be performed to improve the composite properties and healing efficiency by improving the quality of the healing carriers (core−shell nanofibers).

ASSOCIATED CONTENT

Supporting Information

The Supporting Information is available free of charge at https://pubs.acs.org/doi/10.1021/acsomega.2c05496.

FESEM images and EDX analysis of pure PVDF and PAN (PDF)

AUTHOR INFORMATION

Corresponding Authors

Prabhakar M. N. − *The Research Institute of Mechatronics, Changwon National University, Changwon 51140 Gyeongsangnam, South Korea;* orcid.org/0000-0002-5274-5632; Email: dr_prabhakar@changwon.ac.kr

Jung-il Song − *Department of Mechanical Engineering, Changwon National University, Changwon 51140 Gyeongsangnam, South Korea*; Email: jisong@changwon.ac.kr

Authors

Naga Kumar C − *Department of Mechanical Engineering, Changwon National University, Changwon 51140 Gyeongsangnam, South Korea*

Mohamad Tarmizie Hassim − *Department of Smart Manufacturing Engineering, Changwon National University, Changwon 51140 Gyeongsangnam, South Korea*

Complete contact information is available at: https://pubs.acs.org/10.1021/acsomega.2c05496

Notes

The authors declare no competing financial interest.

The raw/processed data required to reproduce these findings can be shared.

ACKNOWLEDGMENTS

The Basic Science Research Program supported this work through the National Research Foundation of Korea (NRF) grant funded by the Ministry of Science Education (2021R1A2B5B03002355 and 2018R1A6A1A03024509).

REFERENCES

(1) Du, Y.; Song, C.; Xiong, J.; Wu, L. Fabrication and mechanical behaviors of carbon fiber reinforced composite foldcore based on curved-crease origami. *Compos. Sci. Technol.* **2019**, *174*, 94−105.

(2) Wang, F. S.; Zhang, Y.; Ma, X. T.; Wei, Z.; Gao, J. F. Lightning ablation suppression of aircraft carbon/epoxy composite laminates by metal mesh. *J. Mater. Sci. Technol.* **2019**, *35*, 2693−2704.

(3) Bae, J.-H.; Lee, S.-W.; Chang, S.-H. Characterization of low-velocity impact-induced damages in carbon/epoxy composite laminates using a poly (vinylidene fluoride−trifluoroethylene) film sensor. *Composites, Part B* **2018**, *135*, 189−200.

(4) Gholizadeh, A.; Najafabadi, M. A.; Saghafi, H.; Mohammadi, R. Considering damages to open-holed composite laminates modified by nanofibers under the three-point bending test. *Polym. Test.* **2018**, *70*, 363−377.

(5) Tsilimigkra, X.; Baltopoulos, A.; Tsantzalis, S.; Kotrotsos, A.; Siakavellas, N.; Kostopoulos, V.; Florez, S. Strategies on implementing a potential self-healing functionality in a composite structure. *Cienc. Tecnol. Mater.* **2016**, *28*, 147−154.

(6) Zhu, Y.; Ye, X. J.; Rong, M. Z.; Zhang, M. Q. Self-healing glass fiber/epoxy composites with polypropylene tubes containing self-

pressurized epoxy and mercaptan healing agents. *Compos. Sci. Technol.* **2016**, *135*, 146−152.
(7) Navarchian, A. H.; Najafipoor, N.; Ahangaran, F. Surface-modified poly (methyl methacrylate) microcapsules containing linseed oil for application in self-healing epoxy-based coatings. *Prog. Org. Coat.* **2019**, *132*, 288−297.
(8) Daelemans, L.; Kizildag, N.; Van Paepegem, W.; D'hooge, D. R.; De Clerck, K. Interdiffusing core-shell nanofiber interleaved composites for excellent Mode I and Mode II delamination resistance. *Compos. Sci. Technol.* **2019**, *175*, 143−150.
(9) Tan, P. S.; Somashekar, A. A.; Casari, P.; Bhattacharyya, D. Healing efficiency characterization of self-repairing polymer composites based on damage continuum mechanics. *Compos. Struct.* **2019**, *208*, 367−376.
(10) Champagne, J.; Pang, S.-S.; Li, G. Effect of confinement level and local heating on healing efficiency of self-healing particulate composites. *Composites, Part B* **2016**, *97*, 344−352.
(11) White, S. R.; Sottos, N. R.; Geubelle, P. H.; Moore, J. S.; Kesser, M. R.; Sriram, S. R.; Brown, E. N.; Viswanathan, S. Autonomic healing of polymer composites. *Nature* **2001**, *409*, 794−817.
(12) Ahangaran, F.; Hayaty, M.; Navarchian, A. H.; Pei, Y.; Picchioni, F. Development of self-healing epoxy composites via incorporation of microencapsulated epoxy and mercaptan in poly (methyl methacrylate) shell. *Polym. Test.* **2019**, *73*, 395−403.
(13) Zhang, H.; Wang, P.; Yang, J. Self-healing epoxy via epoxy − amine chemistry in dual hollow glass bubbles. *Compos. Sci. Technol.* **2014**, *94*, 23−29.
(14) Williams, G. J.; Bond, I. P.; Trask, R. S. Compression after impact assessment of self-healing CFRP. *Composites, Part A* **2009**, *40*, 1399−1406.
(15) Mohammadi, M. A.; Eslami-Farsani, R.; Ebrahimnezhad-Khaljiri, H. Experimental investigation of the healing properties of the microvascular channels-based self-healing glass fibers / epoxy composites containing the three-part healant. *Polym. Test.* **2020**, *91*, No. 106862.
(16) Pittala, R. K.; Dhanaraju, G.; Ben, B. S.; Ben, B. A. Self-healing of matrix cracking and delamination damage assessment in microcapsules reinforced carbon fibre epoxy composite under flexural loading. *Compos. Struct.* **2022**, *291*, No. 115691.
(17) Sinha-Ray, S.; Pelot, D. D.; Zhou, Z. P.; Rahman, A.; Wu, X. F.; Yarin, A. L. Encapsulation of self-healing materials by coelectrospinning, emulsion electrospinning, solution blowing and intercalation. *J. Mater. Chem.* **2012**, *22*, 9138−9146.
(18) Neisiany, R. E.; Lee, J. K. Y.; Khorasani, S. N.; Ramakrishna, S. Towards the development of self-healing carbon/epoxy composites with improved potential provided by efficient encapsulation of healing agents in core-shell nanofibers. *Polym. Test.* **2017**, *62*, 79−87.
(19) Kumar, C. N.; Prabhakar, M. N.; Jung-il, S. PVDF green nano fi bers as potential carriers for improving self -healing and mechanical properties of carbon fiber/epoxy prepregs. *Nanotechnol. Rev.* **2022**, *11*, 1890−1900.
(20) Ruan, S.; Wei, S.; Gong, W.; Li, Z.; Gu, J.; Shen, C. "Strengthening, toughening, and self-healing for carbon fiber/epoxy composites based on PPESK electrospun coaxial nanofibers. *J. Appl. Polym. Sci.* **2020**, *138*, No. 50063.
(21) Torkamani, A. E.; Syahariza, Z. A.; Norziah, M. H.; Wan, A. K. M.; Juliano, P. Encapsulation of polyphenolic antioxidants obtained from Momordica charantia fruit within zein/gelatin shell core fibers via coaxial electrospinning. *Food Biosci.* **2018**, *21*, 60−71.
(22) Ma, Y.; Teng, A.; Zhao, K.; Zhang, K.; Zhao, H.; Duan, S.; Li, S.; Guo, Y.; Wang, W. A top-down approach to improve collagen film's performance: The comparisons of macro, micro and nano sized fibers. *Food Chem.* **2020**, *309*, No. 125624.
(23) Al-Ajrash, S. M. N.; Lafdi, K. The role of carbon and SiC crystallinities in the oxidation and mechanical property improvement of hybrid nano-fibers. *Ceram. Int.* **2019**, *45*, 7286−7294.
(24) Kostopoulos, V.; Kotrotsos, A.; Sousanis, A.; Sotiriadis, G. Fatigue behaviour of open-hole carbon fibre/epoxy composites containing bis-maleimide based polymer blend interleaves as self-healing agent. *Compos. Sci. Technol.* **2019**, *171*, 86−93.
(25) Kim, S. Y.; Lim, T.-W.; Sottos, N. R.; White, S. R. Manufacture of carbon-fiber prepreg with thermoplastic/epoxy resin blends and microencapsulated solvent healing agents. *Composites, Part A* **2019**, *121*, 365−375.
(26) Neisiany, R. E.; Lee, J. K. Y.; Khorasani, S. N.; Ramakrishna, S. Self-healing and interfacially toughened carbon fibre-epoxy composites based on electrospun core−shell nanofibres. *J. Appl. Polym. Sci.* **2017**, *134*, No. 44956.
(27) Wang, H.; Cai, H.; et al. Research on core-shell nanofiber self-healing composites for structural applications. *Polym. Compos.* **2021**, *42*, 3281−3292.
(28) Chen, B.; Zhang, Y.; Mao, C.; Gan, Y.; Li, B.; Cai, H. Research on electrospinning thermosetting-thermoplastic core-shell nanofiber for rapid self-healing of carbon fiber/epoxy composites. *Compos. Sci. Technol.* **2022**, *227*, No. 109577.
(29) Jaswal, S.; Gaur, B. New trends in vinyl ester resins. *Rev. Chem. Eng.* **2014**, *30*, 567−581.
(30) Russo, P.; Nasti, G.; Coppala, S.; Gentile, G.; Tuccitto, N.; Li-Destri, G.; Marletta, G.; Ferraro, P. Single fibres of pyro-electrospinned PVDF-HFP/MWCNT unveal high electrical conductivity. *Polymer* **2018**, *159*, 157−161.
(31) Saxena, P.; Shukla, P. A comprehensive review on fundamental properties and applications of poly (vinylidene fluoride) (PVDF). *Adv. Compos. Hybrid Mater.* **2021**, *4*, 8−26.
(32) Wang, Z.; Sahadevan, R.; Crandall, C.; Menkhaus, T. J.; Fong, H. Hot-pressed PAN/PVDF hybrid electrospun nanofiber membranes for ultrafiltration. *J. Membr. Sci.* **2020**, *611*, No. 118327.
(33) Hübner, F.; Meuchelböck, J.; Wolff-Fabris, F.; Mühlbach, M.; Altstädt, V.; Ruckdäschel, H. Fast curing unidirectional Carbon Epoxy Prepregs based on a Semi-latent Hardener: The Influence of Ambient Aging on the Prepregs Tg0, Processing Behavior and thus derived Interlaminar Performance of the Composite. *Compos. Sci. Technol.* **2021**, No. 109047.
(34) Pinto, T. V.; Cardoso, N.; Costa, P.; Sousa, C. M.; Duraes, N.; Silva, C.; Coelho, P. J.; Pereira, C.; Freire, C. Light driven PVDF fibers based on photochromic nanosilica@ naphthopyran fabricated by wet spinning. *Appl. Surf. Sci.* **2019**, *470*, 951−958.
(35) Merlini, C.; Barra, G. M. O.; Araujo, T. M.; Pegoretti, A. Electrically pressure sensitive poly (vinylidene fluoride)/polypyrrole electrospun mats. *RSC Adv.* **2014**, *4*, 15749−15758.
(36) Cai, X.; Lei, T.; Sun, D.; Lin, L. A critical analysis of the α, β and γ phases in poly (vinylidene fluoride) using FTIR. *RSC Adv.* **2017**, *7*, 15382−15389.
(37) Pan, W.; He, X. W.; Chen, Y. Preparation and characterization of polyacrylonitrile-polyaniline blend nanofibers. *Appl. Mech. Mater.* **2011**, *44*, 2195−2198.
(38) Cavallo, G.; Metrangolo, P.; Milani, R.; Pilati, T.; Priimagi, A.; Resnati, G.; Terraneo, G. The halogen bond. *Chem. Rev.* **2016**, *116*, 2478−2601.
(39) Anvari, A.; Yancheshme, A. A.; Rekaabdar, F.; Hemmati, M.; Tavakolmoghadam, M.; Safekordi, A. PVDF/PAN blend membrane: preparation, characterization and fouling analysis. *J. Polym. Environ.* **2017**, *25*, 1348−1358.

https://doi.org/10.1021/acsomega.2c05496
ACS Omega 2022, 7, 42396−42407